PAPER

Bi-doped CoTe nanoparticles for nonlinear and optoelectronic applications

S. Supriya,[a] Gangamani Tudu,[b] Prabhukrupa C. Kumar, [ID][a] M. Pradhan[c] and R. Naik [ID] *[a]

The exceptional properties and broad applicability of CoTe nanoparticles make them highly relevant for various technological applications, particularly in optoelectronics. Introducing a metal dopant into a nanomaterial matrix has been shown to enhance its characteristics, thereby expanding its potential use. This study presents a straightforward hydrothermal synthesis method for Bi-doped CoTe nanoparticles, wherein four different samples were synthesized by varying the Bi doping concentration. Structural characterization *via* X-ray diffraction confirmed the presence of the hexagonal CoTe phase, with noticeable phase shifts attributed to Bi incorporation. Raman spectroscopy provided insights into the vibrational modes of CoTe, while transmission electron microscopy further verified the CoTe phase and measured interplanar spacing. A field emission scanning electron microscopy morphological study revealed a constant nanoparticle-like structure that did not alter as the concentration of Bi increased. Elemental composition was examined through X-ray photoelectron spectroscopy, confirming the composition of the expected material. Additionally, UV-Vis spectroscopy revealed a bandgap reduction in the range of 3.35–1.64 eV, suggesting modifications in the material's optical properties. Meanwhile, the refractive index value of the material gradually increased in the range of 2.00–3.08. The photoresponse study showed a photocurrent ranging from 229 to 810 µA, with the highest observed in the Bi-3 sample. Additionally, a maximum nonlinear absorption coefficient (β) of 1.448 cm W^{-1} was recorded. These results indicate the material's strong potential for nonlinear photonics and optoelectronic applications.

1. Introduction

Owing to a higher surface area-to-volume ratio, quantum confinement effects, and the tunability of their electronic structures at the nanoscale, nanomaterials exhibit different physical and chemical properties from their bulk counterparts.[1] Their large surface area-to-volume ratio and compact size confer them with special qualities. They are, therefore, highly sought after for a number of applications in fields such as electronics, energy, and optoelectronics.[2] Chalcogenide materials can have crystalline, amorphous, or nanocrystalline structures, among other types, and are recognised for their exceptional optical behaviour, electrical conductivity, and semiconductor properties.[3–5]

Chalcogenide materials have significant potential for a variety of uses. They have garnered a lot of interest in a number of emerging fields, including photovoltaic systems, sensing technologies, phase-change memory (PCM) devices, and photocatalytic processes.[6–8] Tellurium belongs to the chalcogen group, which also comprises polonium, oxygen, sulfur, selenium. It is categorised as a p-type semiconductor.[9] Due to its advantageous physical and chemical characteristics, tellurium (Te) has garnered a lot of interest in semiconductor research. It is an appropriate choice for low-energy optoelectronic and infrared applications due to its significant narrow direct bandgap of about 0.33 eV at room temperature.[10] Furthermore, the material's performance properties are improved by its anisotropic crystal structure, which makes it appropriate for a range of devices. Although tellurium is classified as a rare element, established extraction and recovery methods enable its production in sufficient quantities to meet the demands of semiconductor and optoelectronic applications. Additionally, tellurium exhibits higher environmental stability than many other semiconductor materials, contributing to the enhanced longevity and reliability of devices fabricated with it.[11]

Metal tellurides, notably CoTe, NiTe, Cu$_2$Te, and others, have drawn interest because of their potential uses in a variety of industries.[12] These materials can be utilized in numerous

[a]Department of Engineering and Materials Physics, Institute of Chemical Technology-Indian Oil Odisha Campus, Bhubaneswar, 751013, India.
E-mail: ramakanta.naik@gmail.com
[b]Physics Department, Utkal University, Vani Vihar, Bhubaneswar, 751004 Odisha, India
[c]Department of Physics, KIIT deemed to be University, Bhubaneswar, 751024 Odisha, India

ways and not only can they be found in different stoichiometries, but they can also be synthesized by a number of methods.[13] These methods include hydrothermal synthesis, microwave irradiation, chemical vapor deposition (CVD) and sol–gel.[14–17] Additionally, numerous studies describe the hydro/solvothermal method of producing cobalt telluride (CoTe), which yields particles of varying sizes and shapes. The final appearance of the particles is determined by a number of variables, including temperature, solvent type, and the amounts of starting materials. CoTe has garnered a lot of interest due to its intriguing structural, electrical, and magnetic properties, which offer potential applications in a variety of sectors.[18] Moreover, this can also be achieved by synthesizing it by various methods and characterizing its various properties. CoTe has become a material with enormous potential due to its extensive electronic structure, thermal stability, and semiconducting properties. The electrical, optical, and catalytic properties of CoTe can be further modulated by doping it with right elements, which makes it a desirable option for multipurpose applications.[19] However, doping CoTe with appropriate metal atoms like Bi, Zn, Sb, and In can greatly improve its electrical and optical characteristics, making it easier to develop a variety of electronic and optoelectronic devices.[20] M. S. Khan et al.[21] prepared cobalt telluride superstructures via hydrothermal synthesis method to study the visible light photoconversion of carbon dioxide into methane. This material can also serve as a photocatalyst under visible light irradiation and for photoreduction of CO_2 into CH_4. Meanwhile, CoTe and $NiTe_2$ have also been employed as Pt-free counter electrodes (CEs) in dye-sensitized solar cells (DSCs) by J. Guo et al.,[22] indicating a cost-effective alternative to metal Pt. However, by doping with various metals and semimetals like Bi, In, Ni, and Zn, the physical and chemical properties of the crystal lattice can be enhanced in various ways.[23] Bi doping modifies a variety of nanomaterial characteristics.

Bi doping can efficiently modify the electronic band structure of CoTe, possibly reducing the bandgap and improving light absorption in the visible and near-infrared spectra. Bi doping can also improve photogenerated charge separation and transport, which are both essential for photodetector performance, by raising carrier concentration and mobility. Furthermore, incorporating Bi is also known to enhance responsivity, detectivity, and reaction time while lowering recombination rates.[24] The ionic radius of Bi causes changes in the structural parameters, and doping concentrations alter the optical and electrical properties. To alter the electrical properties and improve performance in applications like thermoelectrics and optoelectronics, Bi can be doped with a variety of substances.[25] Bi-doped CoTe nanoparticles have attracted interest because of their possible uses in solar energy harvesting and thermoelectric devices. Many researchers have investigated this material for its application in energy storage devices. J. Tabassum et al.[26] employed Bi-doped CoTe evaporators for solar-driven desalination, where Bi enhanced the surface plasmonic effect of CoTe after doping. In addition, a small amount of Bi doping showed a solar efficiency of 96.7%

with a water flux of 2.38 kg m^{-2} h^{-1}. Furthermore, the doping of Bi has also been performed for the synthesis, characterization, and photocatalytic performance of Bi_2O_3-doped WO_3 nanoparticles decorated on reduced graphene oxide (rGO) sheets—a highly conductive, two-dimensional carbon-based material—by Z. M. Alaizeri et al.[27] The results also demonstrated the improved properties after the doping of Bi. Numerous studies have been conducted focusing on energy storage and related applications; however, comprehensive characterization techniques, such as optical analyses, are still lacking and remain to be explored.[28]

Additionally, hydrothermal synthesis, a popular technique for producing nanomaterials using solution-based reactions, allows a wide temperature range from room temperature to extremely high temperatures.[29] This method has worked well for producing a variety of nanomaterials by modifying the pressure conditions according to the vapour pressure of the primary formulation. Its benefits include the production of materials that are unstable at high temperatures and the efficient synthesis with minimal material loss.[30]

Inspired by the previously mentioned studies, herein, the hydrothermal synthesis method has been employed to prepare a CoTe crystal lattice in which different amounts of Bi have been doped. Various Bi concentrations have been examined, and different nanomaterials have been developed. The crystalline phase and a phase shift towards higher angles were revealed by the structural analysis of the material, while the Raman spectra demonstrated several vibrational bonds in the crystal lattice. The morphological analysis confirmed the nanoparticle-like structure of the material. Additionally, the material's thermal behaviour was demonstrated by DSC measurements, and the optical properties were examined using UV-Vis spectroscopy.

2. Experimental

2.1 Materials and experiment

The following materials were used as starting materials: cobalt chloride hexahydrate ($CoCl_2·H_2O$) (98%, GLR Innovations), bismuth(III) nitrate pentahydrate ($Bi(NO_3)_3·5H_2O$) (99.99%, Sigma Aldrich), sodium tellurite (Na_2TeO_3), and deionized water. Hydrazine hydrate ($N_2H_4·H_2O$) was used as the reducing agent. All materials were used without any additional purification. The Bi-doped CoTe samples were synthesized using the hydrothermal method. Initially, a precursor solution was prepared by dissolving 1 mmol of $CoCl_2·H_2O$ and 1 mmol of Na_2TeO_3 in 70 ml of deionized (DI) water. To facilitate reduction, 10 ml of $N_2H_4·H_2O$ was added to the solution. The mixture was then stirred continuously for 2 hours to ensure uniform distribution of the components. After thorough mixing, the solution was transferred into a 100 ml Teflon-lined stainless steel autoclave. The undoped sample, named CoTe, was synthesized under hydrothermal conditions at 200 °C for 24 hours. Following the successful synthesis of the undoped sample, Bi doping was introduced into the precursor solution,

and three additional samples were prepared under identical hydrothermal conditions. The Bi-doped samples, labeled as Bi-1, Bi-2, and Bi-3, contained Bi concentrations of 0.25 mmol, 0.30 mmol, and 0.35 mmol, respectively. The samples were then centrifuged twice with DI water, followed by ethanol at 11 000 rpm, and dried in an oven at 60 °C overnight to obtain the powder sample. A schematic representation of the synthesis process is provided in Scheme 1.

2.2 Material characterization

The structural, morphological, compositional, thermal, and optical properties of the synthesized samples were analysed using various characterization techniques. X-ray diffraction (XRD) patterns were recorded using a Bruker D8 Advance X-ray diffractometer with Cu Kα radiation (λ = 1.54 Å), scanning over a range from 10° to 70°. Raman spectroscopy was performed using a Renishaw RE 04 Raman microscope enclosure system with a 532 nm excitation wavelength, covering the spectral range of 100–400 nm. Morphological analysis was conducted using Field Emission Scanning Electron Microscopy (FESEM) with an Energy Dispersive X-ray (EDX) source (JEOL, JSM 7610F-Plus) to assess the composition of the samples. High-resolution transmission electron microscopy (HRTEM) and selected area electron diffraction (SAED) images were obtained using a JEOL TEM-2100 Plus transmission electron microscope (TEM). Differential scanning calorimetry (DSC) measurements were carried out with a HITACHI DSC7020 system, spanning a temperature range of 30–500 °C at a scan rate of 10 °C min⁻¹.

XPS core-level and survey spectra were obtained using an Axis Ultra, Kratos Analytical, UK apparatus, with Al Kα X-rays (1486.6 eV) under 2×10^{-9} Torr vacuum. The optical properties were evaluated using a Jasco V-770 UV-Vis-NIR spectrophotometer, operating within the wavelength range of 200–1200 nm. Collectively, these analytical techniques provided comprehensive insights into the physical and chemical characteristics of the samples.

2.3 Photoresponse study

For photoresponse measurements, the active layer was prepared by drop-casting a 0.3×0.6 mm^2 area of the Bi-doped CoTe nanoparticle dispersion onto a clean glass substrate. Prior to deposition, each sample solution was ultrasonicated for 30 minutes at a concentration of 0.5 mg mL⁻¹ to ensure uniform dispersion. A volume of 50 µL of the prepared solution was then deposited onto the designated region and subsequently dried at 60 °C for 1 hour to achieve film formation. To establish electrical contacts, silver (Ag) paste was applied to the opposite edges of the dried material. The resulting photodetector (PD) devices were carefully mounted onto a sample holder to ensure optimal exposure to ambient light conditions. For optical excitation, a 9 W UV light source emitting at 370 nm was employed. Current–voltage (I–V) characteristics were measured using a Keithley 2450 Source Meter Unit (SMU) over a bias range from −10 V to +10 V with a step size of 0.05 V. Measurements were carried out under both illuminated and dark conditions to evaluate the photoresponse behaviour of the samples. The experimental setup is shown in Scheme 2.
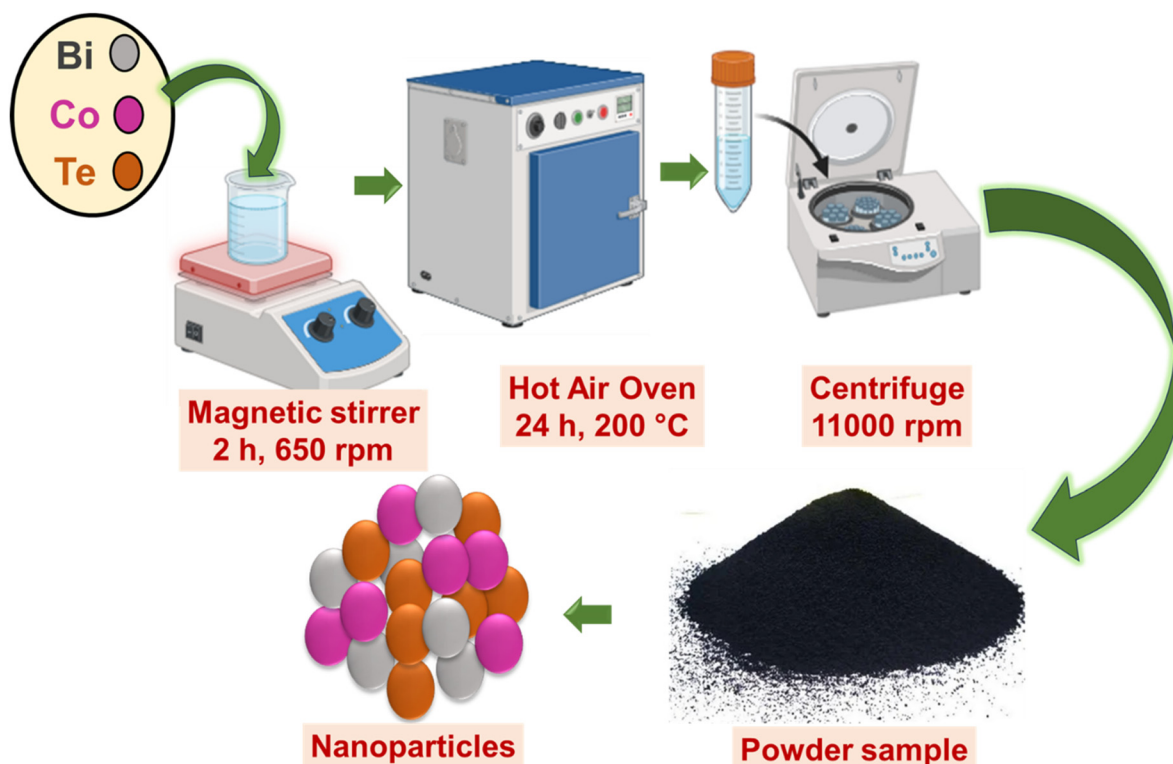
Scheme 1 Schematic representation of the synthesis procedure.
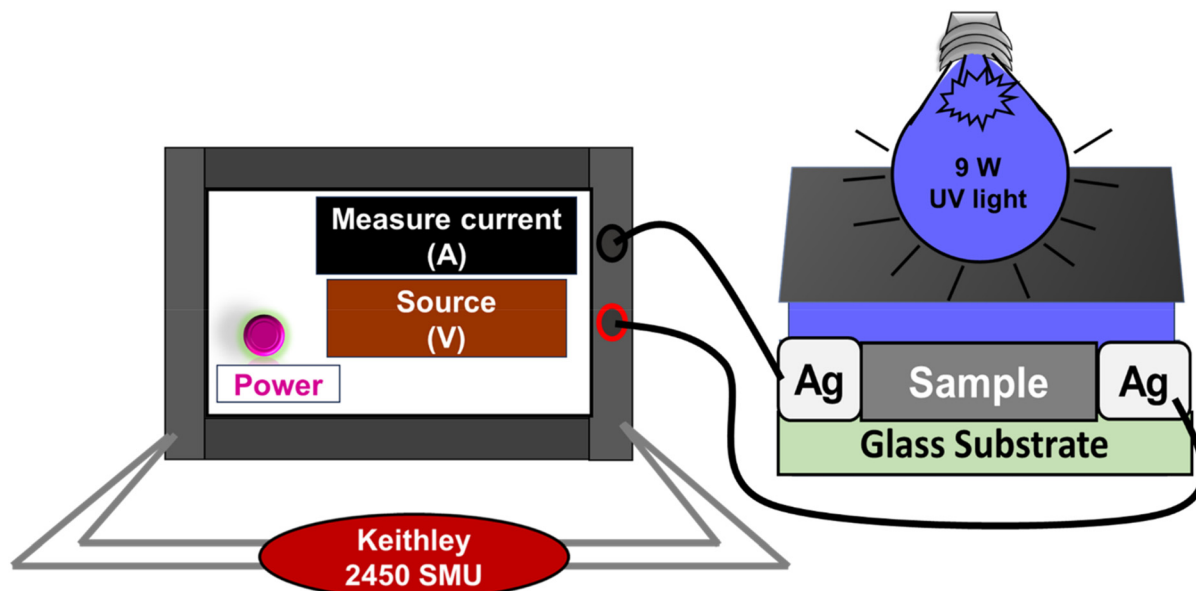
Scheme 2 Schematic depiction of the experimental setup for *I–V* measurements.

2.4 NLO study by the *Z*-scan technique

The nonlinear optical (NLO) properties of the Bi-doped CoTe nanoparticles were investigated using the standard *Z*-scan technique. A commercially available Holmarc *Z*-scan setup (model: HO-ED-LOE-03) was employed to assess the intensity-dependent optical response of the samples. The experimental setup included a motorized linear translation stage with a total travel range of 150 mm and a minimum step resolution of 0.1 mm, allowing precise movement of the sample along the *Z*-axis. A diode-pumped solid-state (DPSS) laser operating at 532 nm with an output power of 100 mW served as the excitation source. To focus the laser beam, two optical lenses with focal lengths of 100 mm and 286 mm, respectively, were mounted in adjustable lens holders. The Bi-doped CoTe dispersions were contained in a 1 mm path length cuvette, securely held in a cuvette holder during the measurements. The translation stage, controlled *via* a computer interface, enabled accurate positioning of the sample relative to the laser beam focus. The setup incorporated two photodetectors, PD1 and PD2, to monitor the incident and transmitted beam intensities. The measurements were conducted both with and without an aperture in front of PD2 to differentiate between open-aperture (OA) and closed-aperture (CA) configurations. Scheme 3 shows the experimental setup of the *Z*-scan technique.

3. Results and discussion

3.1 XRD analysis

X-ray diffraction (XRD) data have been used to conduct a thorough structural study that includes the crystallite size, lattice strain, dislocation density, and unit cell parameters. The XRD patterns of all the samples have been recorded using
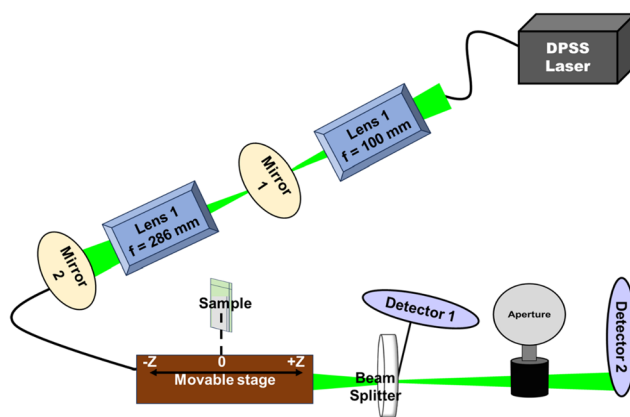
Scheme 3 Schematic illustration of the experimental setup for *Z*-scan measurements.

a Brucker D8 Advanced X-ray diffractometer with Cu Kα radiation (λ = 1.54 Å). The 2theta (2θ) scan range of the measurement was set from 10 °C to 70 °C. Fig. 1(a) shows the XRD patterns of all the samples. It can be observed that the samples exhibit a polycrystalline hexagonal phase of CoTe with the *P*63/*mmc* space group. The 2θ values at 31.37°, 42.54°, 46.52°, and 57.59° have been observed, corresponding to the crystal planes of (101), (102), (110), and (112), respectively for all the samples (doped and undoped), and no secondary phases have been observed (ICSD: 00-034-0420). The unit cell parameters have been determined to be $a = b = 3.89$ Å and $c = 5.37$ Å. The phases have also been studied by M. Manikandan *et al.*,[31] where similar crystal planes have been observed.

The phase shift of the material has also been occurred in the (101) plane and is shown in Fig. 1(b). This shift clearly indicates the shifting of the plane to a higher 2θ value due to
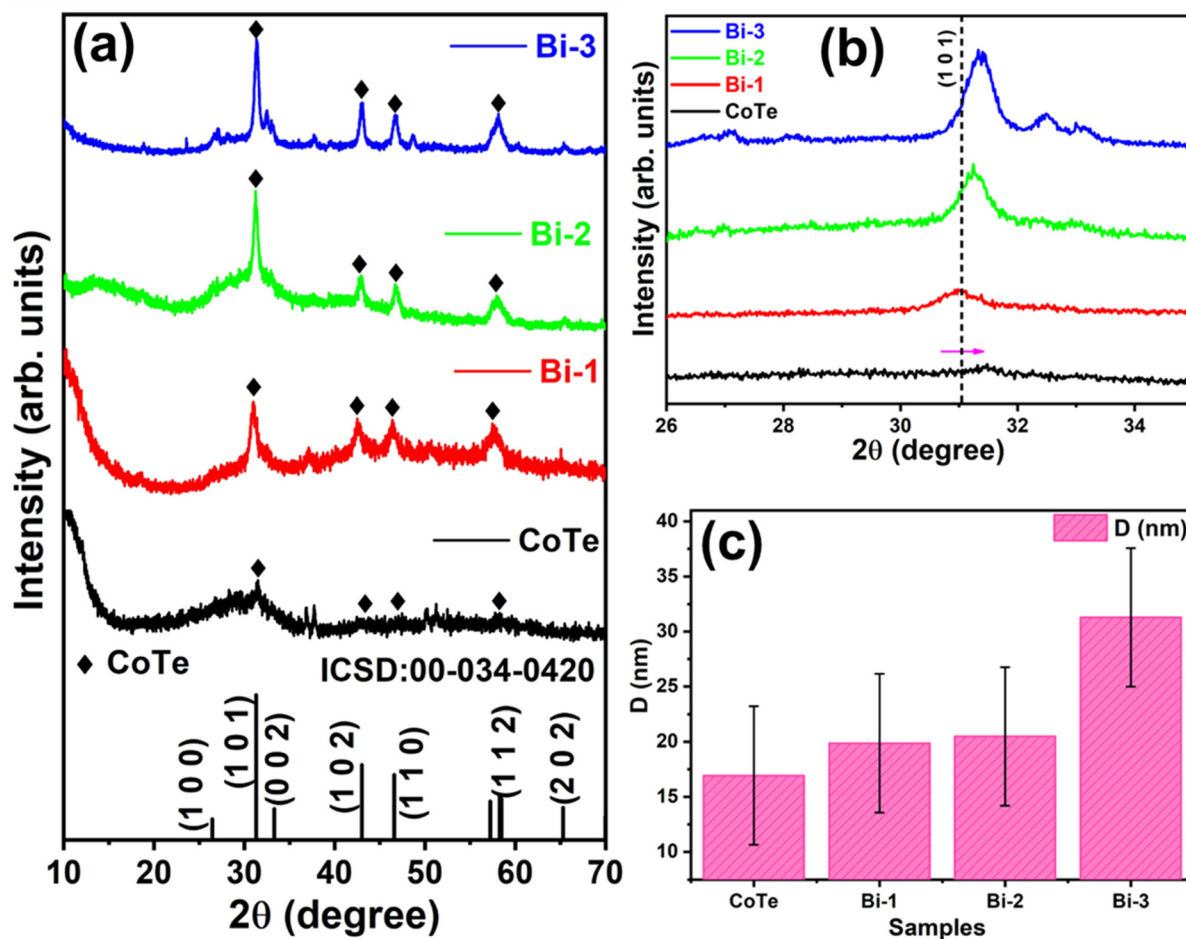
Fig. 1 (a) XRD patterns of all the samples, (b) phase shift of the (101) plane, and (c) variation in the crystallite size (*D*) of the material.

the incorporation of Bi into the CoTe crystal lattice. This might be due to the replacement of lower atomic radii of Bi with the higher atomic radii of Co. The crystallite size (*D*), the lattice strain (ε), and dislocation density (δ) of the samples have also been calculated using various equations. The crystallite size was calculated using the Scherrer equation,[32]

$$D = 0.9\lambda/\beta \cos\theta \quad (1)$$

where θ is the Bragg's angle, β is the full width at half maximum (FWHM), and λ is the wavelength of the Cu Kα line (1.54 Å).

The dislocation density (δ) and lattice strain (ε) have also been calculated using the following relations:[33,34]

$$\delta = 1/D^2 \quad (2)$$

$$\varepsilon = \beta \cot\theta/4 \quad (3)$$

The crystallite size was calculated and found to be increasing with the enhancement of the incorporation of Bi. The values of the crystallite size, dislocation density and lattice strain are provided in Table 1. The increase in the crystallite size of all the samples is also shown in Fig. 1(c), where it can be observed that the crystallinity enhanced after the incorpor-

Table 1 Structural data of all the samples

Sample	Average crystallite size (*D*) (nm)	Dislocation density (δ) ($\times 10^{15}$) m^{-2}	Lattice strain (ε) (nm)$^{-2}$
CoTe	16.929 ± 0.1	0.003 ± 0.0002	0.006 ± 0.002
Bi-1	19.863 ± 0.4	0.002 ± 0.0001	0.005 ± 0.003
Bi-2	20.482 ± 0.3	0.002 ± 0.0001	0.004 ± 0.001
Bi-3	31.279 ± 0.2	0.001 ± 0.00003	0.003 ± 0.002

ation of Bi. In addition, the highest Bi-doped sample, Bi-3, shows very good crystallinity and the highest crystallite size. The values of dislocation density as well as lattice strain have been observed to be decreasing gradually as the Bi content in the material increased.

3.1.1 Williamson–Hall (W–H) method. Another crucial method to calculate the structural parameters such as the crystallite size and lattice strain is the Williamson–Hall (W–H) method. It is evident from eqn (1) that the diffracted angle depends on $1/\cos\theta$. However, the W–H technique depends on $\tan\theta$, which contradicts Scherrer's formula. To determine the lattice stresses and crystallite sizes of the nanoparticles, the W–H plot has been generated. So, this is a comparative

method to the Scherrer equation. The W–H plot of the nanomaterials has been plotted and is shown in Fig. 2(a). It can be noticed that the plot depends on $4 \sin \theta$ and $\beta \cos \theta$. The combined effect of the crystallite size and lattice strain results in the total broadening in XRD peaks. It can be expressed as

$$\beta_T = \beta_D + \beta_\varepsilon \tag{4}$$

where β_T refers to the total broadening, β_ε represents the broadening due to strain and β_D is the broadening due to the crystallite size.[35]

Compared to the Scherrer equation, it can be modified as

$$\beta_T = \frac{K\lambda}{D \cos \theta} + 4\varepsilon \tan \theta. \tag{5}$$

It can also be written as

$$\beta_T \cos \theta = \frac{K\lambda}{D} + 4\varepsilon \sin \theta. \tag{6}$$

Here, ε represents the slope and $\frac{K\lambda}{D}$ refers to the intercept of the straight-line equation.

The crystallite size has also been calculated using this method and found to be 17, 21, 23, and 33 nm for CoTe, Bi-1, Bi-2, and Bi-3, respectively. So, the average crystallite size from both the methods varied by ±3 nm.

3.2 Raman study

The vibrational spectroscopy of CoTe nanomaterials has been studied through Raman spectroscopy.[36] When an input light photon hits a molecule and produces a scattered photon, the technique is known as Raman spectroscopy, which measures the frequency shift of the scattered light from the sample. Their distinct vibrational properties enables highly sensitive structural identification and simple interpretation of tiny quantities of substances.[37] The Raman spectra of all the

samples are shown in Fig. 2(b). The Raman peak positions of Bi-doped and undoped CoTe are similar. However, when comparing the Bi-doped samples with the undoped CoTe, a substantial rise in Raman peak intensity has been observed. This is because Bi doping might enhance Raman scattering by reducing phonon damping, which might result in enhanced local ordering or crystallinity.[38,39] Furthermore, the Raman peaks have been observed at 120 and 139 cm^{-1}. The peak corresponding to 120 cm^{-1} can be attributed to the Te–Te bonds of Te. This suggests the existence of vibrational modes linked to the interactions between tellurium atoms.[40] However, the Raman peak around 139 cm^{-1} can be allocated to the A_g Raman active mode of CoTe, which is associated with the Te vibrations. When atoms move in a phase along a particular axis without altering the structure's overall symmetry, this is known as a symmetric, non-degenerate vibration.[41]

3.3 FESEM and EDX analyses

FESEM is a sophisticated imaging method that scans a sample with a precisely focused electron beam to create high-resolution images using field emission. Moreover, FESEM is the most widely used technology for determining the morphology of the as-prepared material's nanostructures. The FESEM images of all the samples are shown in Fig. 3. The FESEM images of CoTe, Bi-1, Bi-2, and Bi-3 samples at 100 nm are shown in Fig. 3(a–d), respectively. It can be clearly understood that all the samples show nanoparticle-like morphology, and it is unaltered even after enhancing the Bi content in the material. Additionally, Fig. S1 of the SI shows the FESEM image of all the samples at 1 μm magnification.

The particle size has also been calculated for all the samples. The mean particle size of all the samples has been found to be 20, 21, 27 and 32 nm for CoTe, Bi-1, Bi-2, and Bi-3
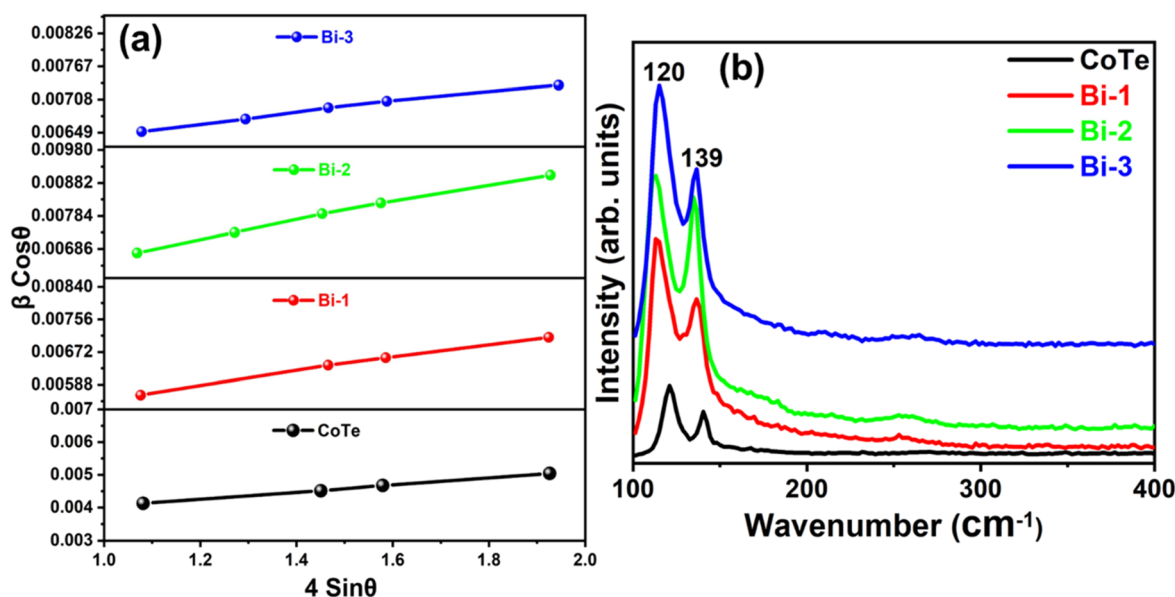

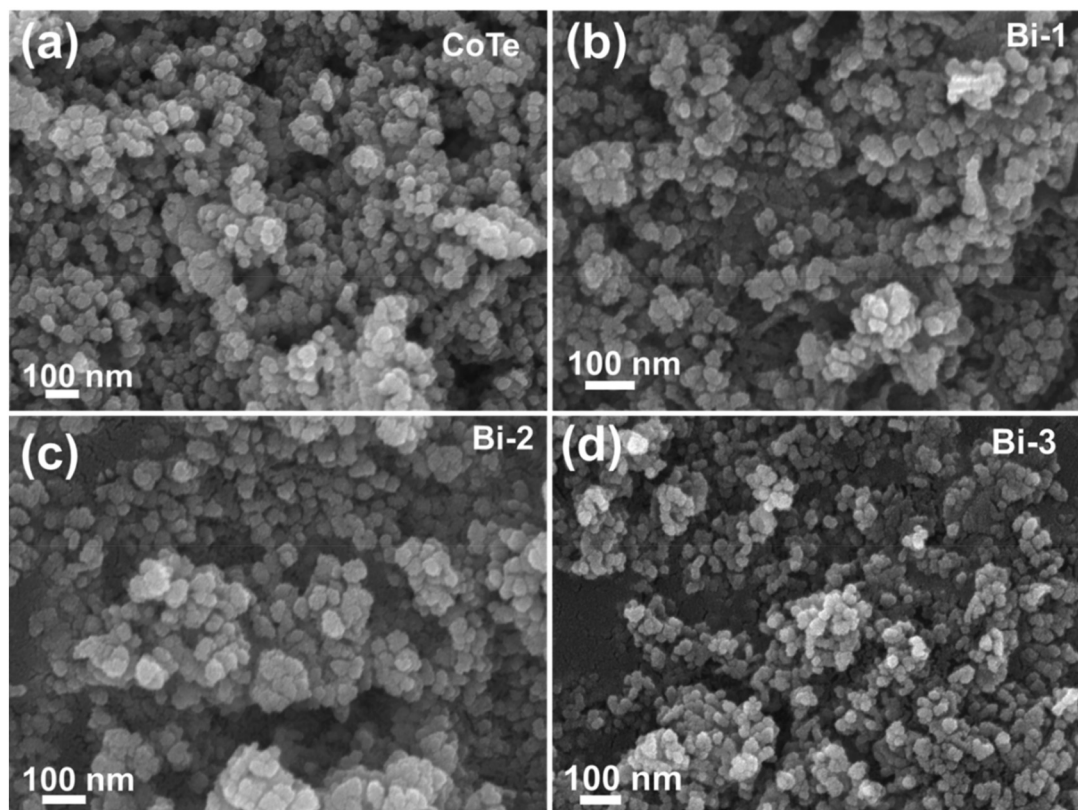**Fig. 2** (a) W–H plot and (b) Raman spectra of the nanomaterials.

Fig. 3 FESEM images of (a) CoTe, (b) Bi-1, (c) Bi-2, and (d) Bi-3 samples.

samples, respectively. The particle size histogram of all the samples is shown in Fig. 4. The particle size has also been observed to be increasing with the increase in the Bi content in the material. The particle size bar that shows the increase in the particle size is shown in Fig. S2 of the SI.

The elemental mapping and the EDX spectrum of the Bi-3 composite nanostructure are shown in Fig. 5. The spatial distribution of the elements in Fig. 5(a–d) is depicted in the elemental mapping, which enables successful element identification. The EDX spectrum shows the presence of Bi, Co, and Te elements, which proves the formation of the Bi-doped CoTe material, as shown in Fig. 5(e). In Fig. 5(e), the peak at 0.67 keV aligns with characteristic X-ray emissions associated with cobalt, which indicates the presence of cobalt (Co) in the nanomaterial. The intensity of the peaks provides insight into the relative concentration of any element compared to other elements present in the sample. The spatial distribution of elements across the nanoparticles' surface is represented using elemental mapping. On the other hand, the elements contained in the sample were represented by distinctive peaks in the EDX spectra.

3.4 TEM analysis

TEM is a highly versatile technique commonly utilized for characterizing nanomaterials due to its exceptional spatial resolution and ability to reveal detailed internal structures of

nanoparticles. TEM analysis was conducted on the Bi-3 sample, as shown in Fig. 6. The TEM images captured at 100 nm and 20 nm, shown in Fig. 6(a) and (b), respectively, further validate the nanoparticle morphology of the material. Additionally, the TEM image of the Bi-3 sample at 50 nm is shown in Fig. S3 of the SI. These images clearly confirm the presence of nanoparticle-like structures, aligning with the findings from the FESEM analysis.

Additionally, Fig. 6(c) displays the high-resolution TEM (HRTEM) image of the sample, where the observed interplanar spacing (d) of 2.1 Å corresponds to the (102) plane of CoTe, while the 2.8 Å spacing is associated with the (101) plane of CoTe. Furthermore, the SAED pattern, as depicted in Fig. 6(d), highlights the crystalline nature of the nanoparticles. The distinct lattice fringes, with spacings of 2.1 Å and 2.8 Å, correspond to the (102) and (101) hexagonal planes of CoTe crystals, thereby corroborating the earlier XRD results.

3.5 XPS study

The surface chemistry of nanomaterials can be investigated using XPS. It offers thorough insights into the elemental composition, chemical states, and electronic structure, all of which are essential for comprehending and improving the characteristics of nanomaterials for a variety of applications.[42] The XPS spectra of the Bi-3 sample are shown in Fig. 7. The survey spectra of the sample are shown in Fig. 7(a) from the 0–1200
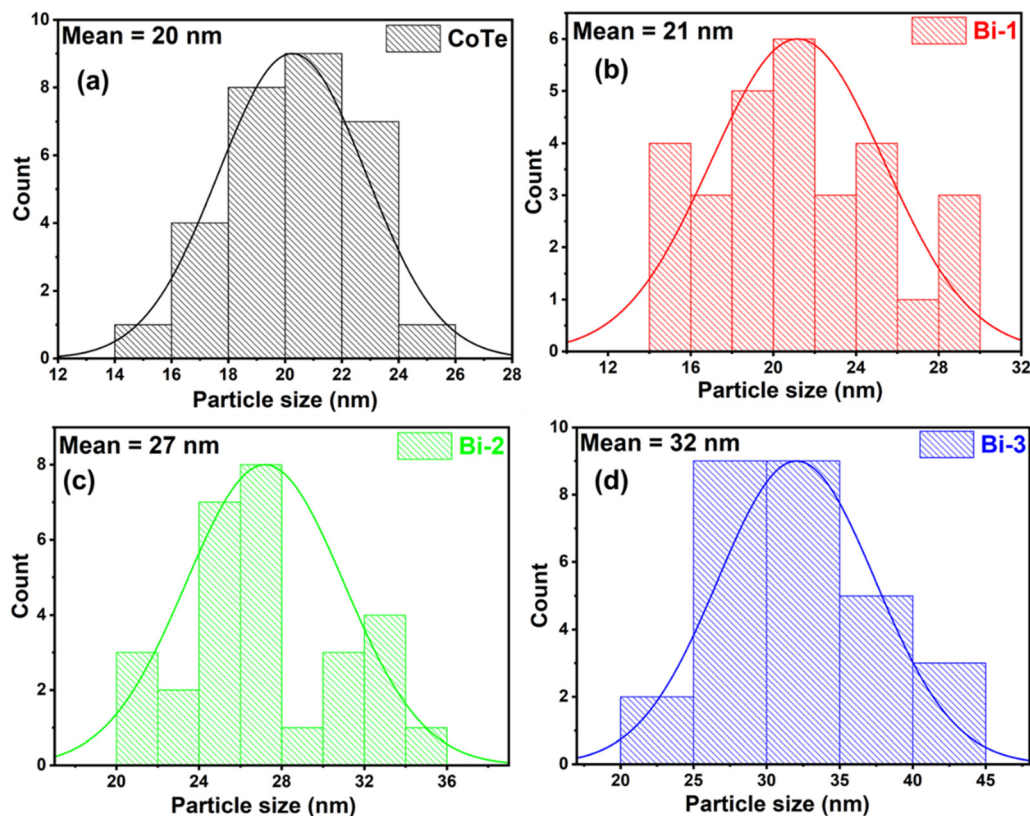
Fig. 4 Particle size histograms of (a) CoTe, (b) Bi-1, (c) Bi-2, and (d) Bi-3 samples.

range, consisting of Co 2p, Te 3d, and Bi 4f, which originate from Bi-doped CoTe. Fig. 7(b), (c), and (d) show the discrete spectra Bi 4f, Co 2p, and Te 3d, respectively. The binding energy values of Bi 4f as seen from Fig. 7(b) are 164.35 eV and 159.09 eV, respectively, which correspond to Bi $4f_{5/2}$ and Bi $4f_{7/2}$. Both the symmetrical wide bands and spin–orbital components are responsible for the intensity ratio of 7/2–5/2. This indicates the Bi^0 and Bi^{3+} content in the material.[43] The Co 2p spectrum shows two main binding energies at 796.97 and 781.03 eV, attributed to Co $2p_{1/2}$ and Co $2p_{3/2}$, respectively, as shown in Fig. 7(c). It can also be observed that the satellite peak is also seen at around 803 and 786 eV.[44,45] Furthermore, Fig. 7(d) depicts the Te 3d plot, in which the Te 3d binding energy peaks can be observed at 586.61 and 576.16 eV for Te $3d_{3/2}$ and Te $3d_{5/2}$, respectively. This is also attributed to Te–Co bonds.[46]

3.6 DSC study

When a sample is heated, cooled, or maintained at a steady temperature, DSC calculates the difference in heat flow between the sample and a reference. Exothermic and endothermic transitions, which correlate to phase changes, are visible in the resulting DSC thermogram (heat flow *vs.* temperature).[47] DSC is a useful technique to analyse the thermal properties of Bi-doped CoTe nanomaterials. The DSC measurement of the Bi-3 sample has been performed, and the

pattern is shown in Fig. 8. It can be clearly seen that one endothermic and one exothermic peak have occurred. The endothermic peak of the material is observed at 267.7 °C, with an enthalpy value of 0.65 J g^{-1}. Additionally, the exothermic peak is also observed at 390.9 °C, with an enthalpy value of −121 J g^{-1}. In addition, the DSC curve for CoTe is shown in Fig. S4 of the SI. The effects of Bi doping on the thermal behaviour of CoTe can be compared, particularly for the sample with higher content, Bi-3. Furthermore, the thermal properties of CoTe are altered by the addition of Bi, as Bi doping-induced modifications in phase stability, defect generation, and lattice structure might be responsible for this shift.[48] The peaks may represent a solid-state transformation or a melting phase transition in CoTe. Although CoTe has a melting point between 600 and 700 °C, phase shifts and other decomposition processes can occur at lower temperatures.[49]

3.7 Optical studies

3.7.1 UV-Vis analysis. One popular method for examining the optical characteristics of nanoparticles is UV-Vis spectroscopy. This method provides crucial information about the band gap energy, electronic structure, and optical absorbance of the nanoparticles.[50] Here, the absorbance and direct optical bandgap of all the materials have been investigated by UV-Vis measurements. The absorbance spectra of the samples were recorded in the wavelength range between 200 and 1200 nm.
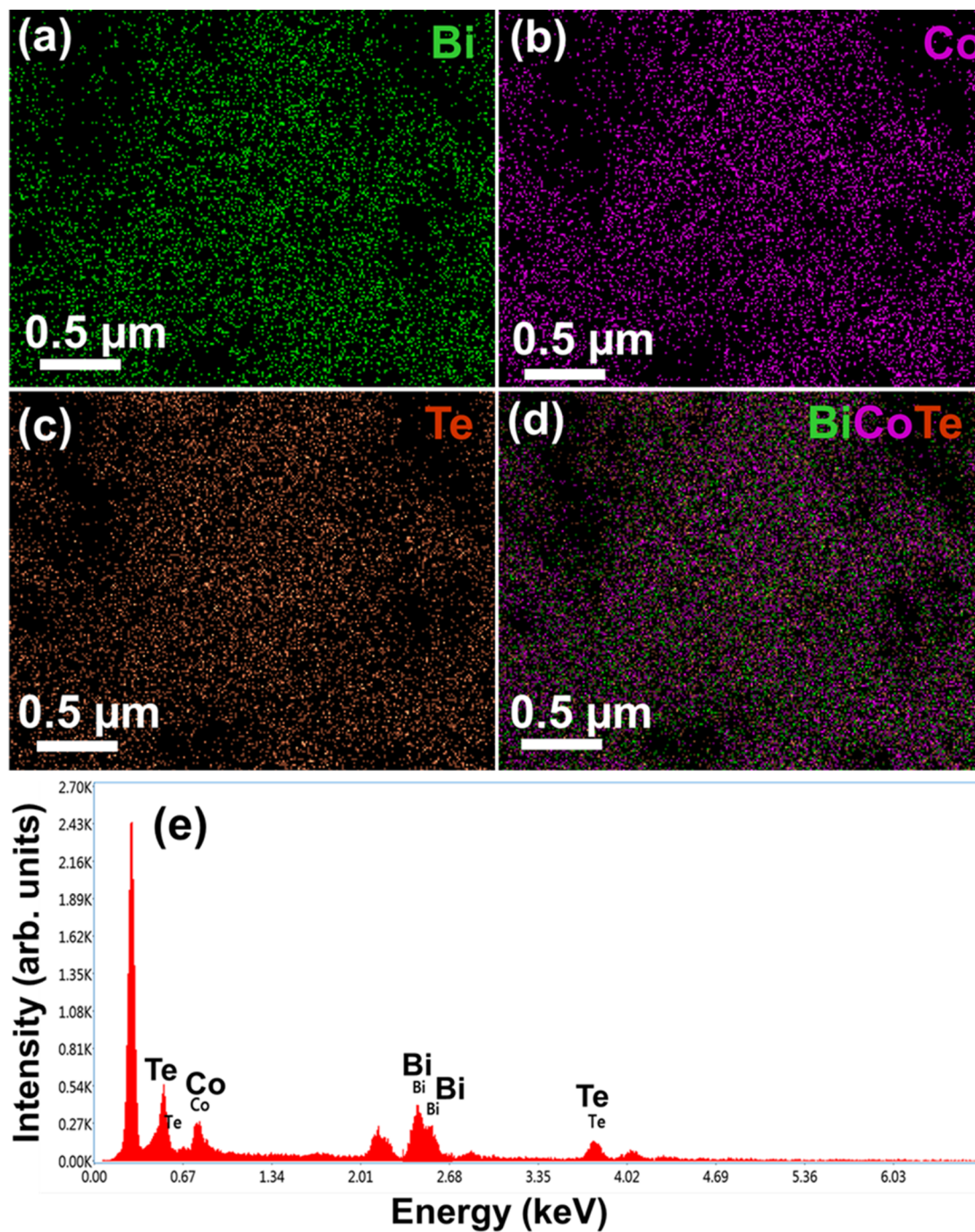
Fig. 5 Elemental mapping of (a) Bi, (b) Co, (c) Te, and (d) BiCoTe, and (e) EDX spectra of the Bi-3 sample.

The UV-Vis analysis is shown in Fig. 9. The absorbance spectra of the material are shown in Fig. 9(a).

The absorption coefficient of the material has been calculated using the equation[51]

$$\alpha = 2.303A \qquad (7)$$

where A represents the absorbance of the material.

It can be observed that the absorbance edge shifts towards a higher wavelength side as the Bi content in the material increases and a red shift has been occurrs.

Additionally, the bandgap of the material has been calculated using the Tauc relation:[52]

$$\alpha h\nu = B(h\nu - E_{\mathrm{g}})^m \qquad (8)$$

where α is the absorption coefficient of the material, h is Planck's constant, and ν is the frequency. Here, B is known as
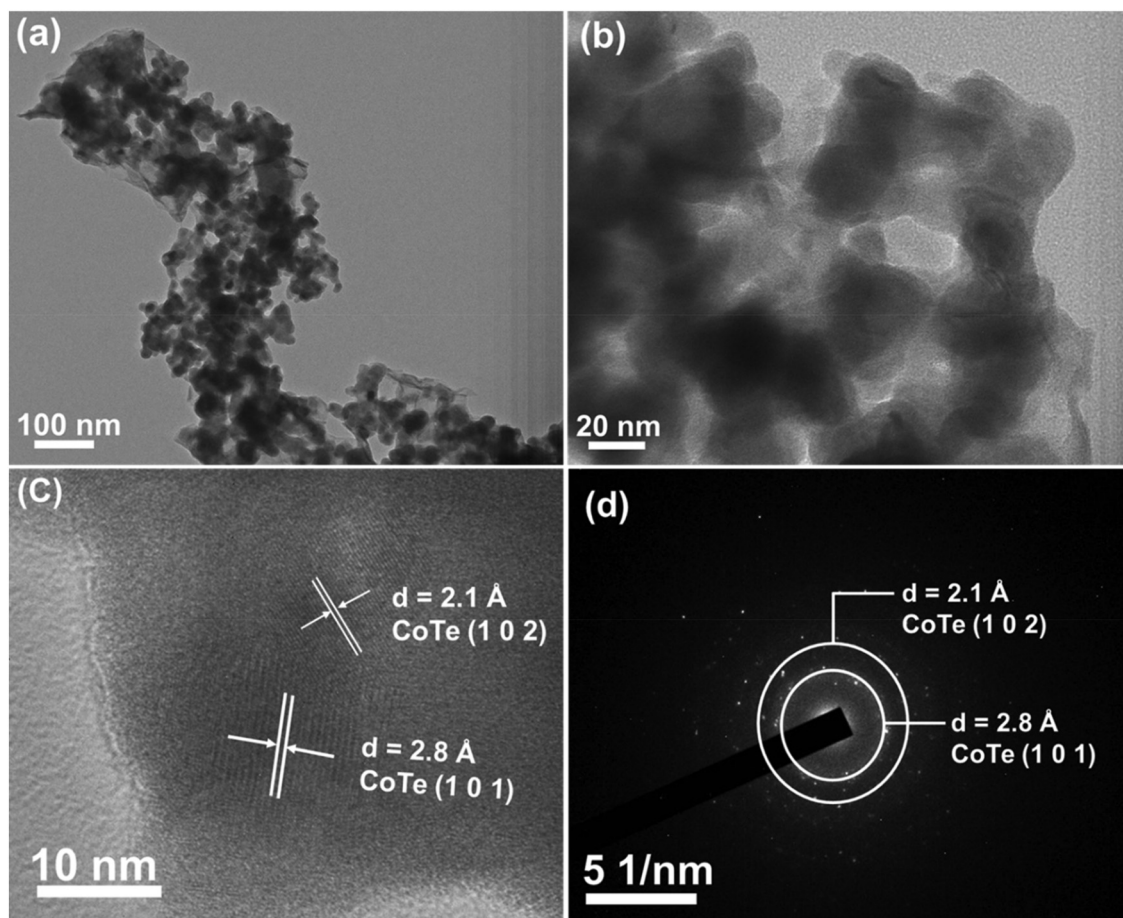
Fig. 6 TEM images at (a) 00 nm and (b) 20 nm, (c) HRTEM image, and (d) SAED pattern of the Bi-3 sample.

a constant, which is related to the transition probability, and E_g refers to the bandgap. Moreover, the values of "*m*" for "direct allowed", "indirect allowed", "indirect forbidden", and "direct forbidden" are, respectively, 1/2, 2, 3, and 3/2. Here, for the calculation of the direct optical bandgap, the value of m has been considered to be $\frac{1}{2}$. The value of E_g was determined by extrapolating the linear region of the $(\alpha h\nu)^2$ *vs.* $h\nu$ graphs. The Tauc plots of all the samples, CoTe, Bi-1, Bi-2, and Bi-3, are shown in Fig. 9(b–e), respectively.

The bandgap energy of all the samples has been calculated and found to be 3.35, 2.33, 2.21, and 1.64 eV for CoTe, Bi-1, Bi-2, and Bi-3 samples, respectively. These values are also provided in Table S1 of the SI. The bandgap of the CoTe material is typically found to be 2.0–2.5 eV.[53] Bi doping might enhance the capacity of the material to absorb NIR photons, thereby opening a pathway for NIR-induced photothermal conversion, as indicated by this redshift in absorption. The significant band gap narrowing and enhanced light absorption properties strongly indicate that Bi-2 and specifically Bi-3 samples are promising candidates for NIR-responsive applications, including photothermal conversion.[54] Moreover, it has also been noticed that with an increase in the Bi content of the material, the E_g value of the material is reduced. This might be due to

the incorporation of the Bi atom into the CoTe crystal lattice. However, the more probable possibilities for the band gap reduction with Bi doping might be lattice strain, defect creation caused by Bi atoms or electronic structure modulation as a result of Bi incorporation.[55,56]

3.7.1 Refractive index and bandgap relation. A crucial factor in optical physics that determines how light moves through various materials is the refractive index (n). It affects several different phenomena, including dispersion, absorption, refraction, and reflection. This characteristic has significance for creating sophisticated photonic materials, designing optical components, and refining semiconductor devices for high-performance applications.[57] The relationship between the bandgap energy and the refractive index in semiconductors has been the subject of extensive studies because it could potentially find use in the optoelectronic sector.[58] To find out the refractive index of the material using the bandgap energy value, many formulas have been proposed by scientists. Among these, Moss gave a semi empirical formula to find out the refractive index value. The Moss rule offers a quick and efficient method for calculating a semiconductor's refractive index from its band gap energy. It is extensively employed in materials science and semiconductor physics, although it has
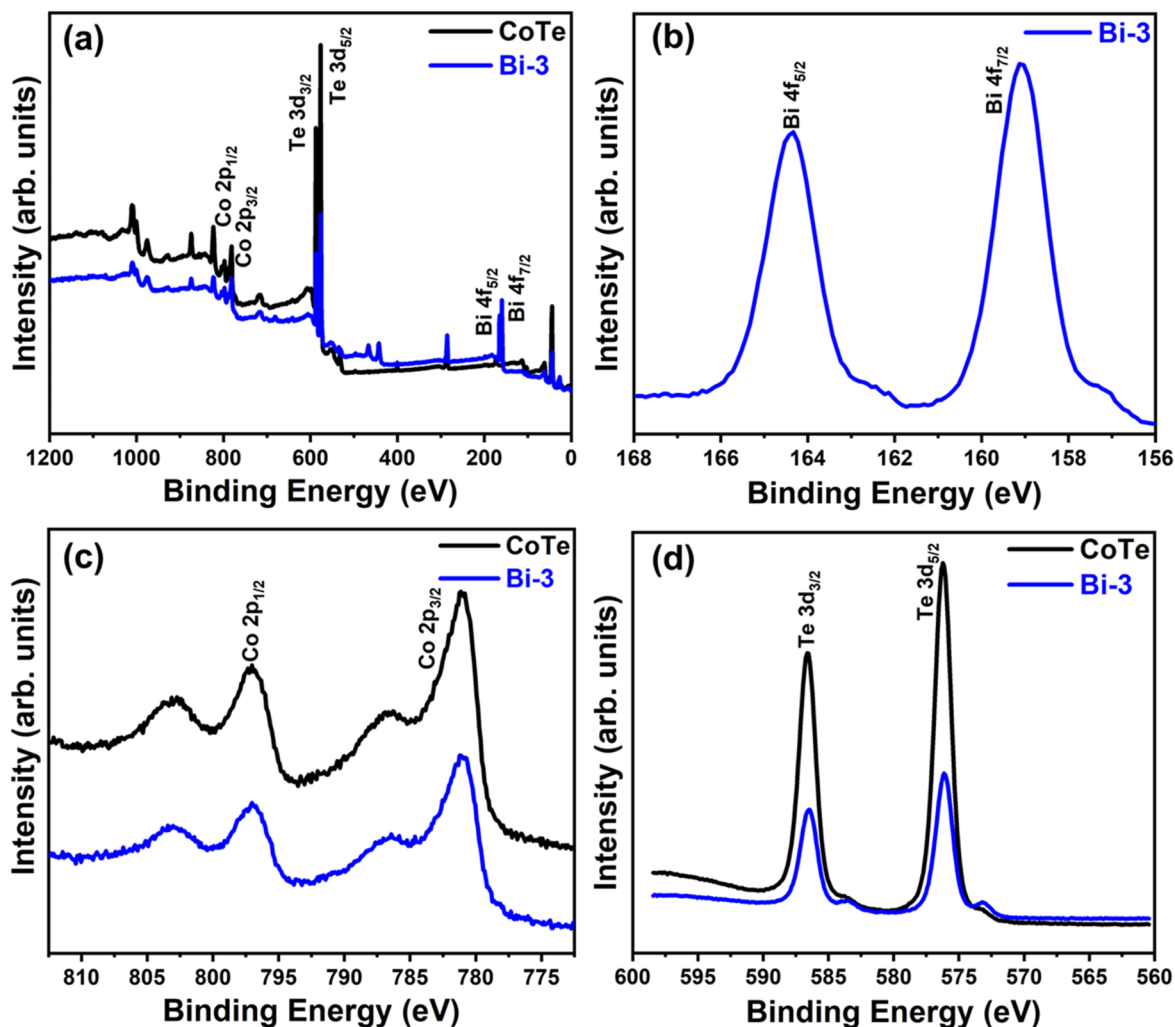
Fig. 7 XPS (a) survey spectra, (b) Bi 4f, (c) Co 2p, and (d) Te 3d of the Bi-3 sample.
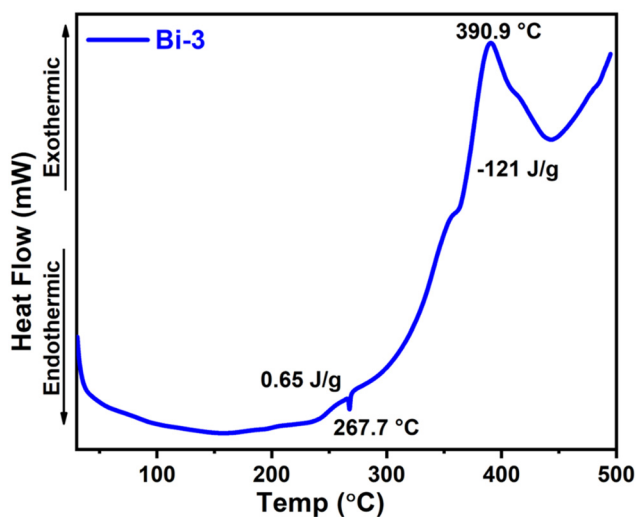

Fig. 8 DSC pattern of the Bi-3 sample.

several drawbacks when utilised with complicated materials. When determining the refractive index at standard optical frequencies using just the band gap energy, the Moss rule is especially helpful.[59] However, a straightforward but efficient technique for determining the refractive index of optical materials based on their band gap is the Dimitrov and Sakka model. It is especially helpful for semiconductors, thin films, and nanomaterials because of its linear dependence on $1/E_g$. Despite being empirical, it is a useful tool in photonics, optoelectronics, and materials science.[60] Similarly, using simply the band gap energy, the Ravindra model offers a simple and useful way to predict the refractive index of semiconductors and optical materials. It is computationally simple and helpful for initial optical material investigation due to its linear relationship between n and E_g.[61] In addition, the Herve & Vandamme and Tripathy models both provide useful techniques for calculating the refractive index based on the optical band gap. For a wider variety of materials, the Tripathy model offers a more explicit power-law approximation, whereas the Herve & Vandamme model is more accurate for semi-
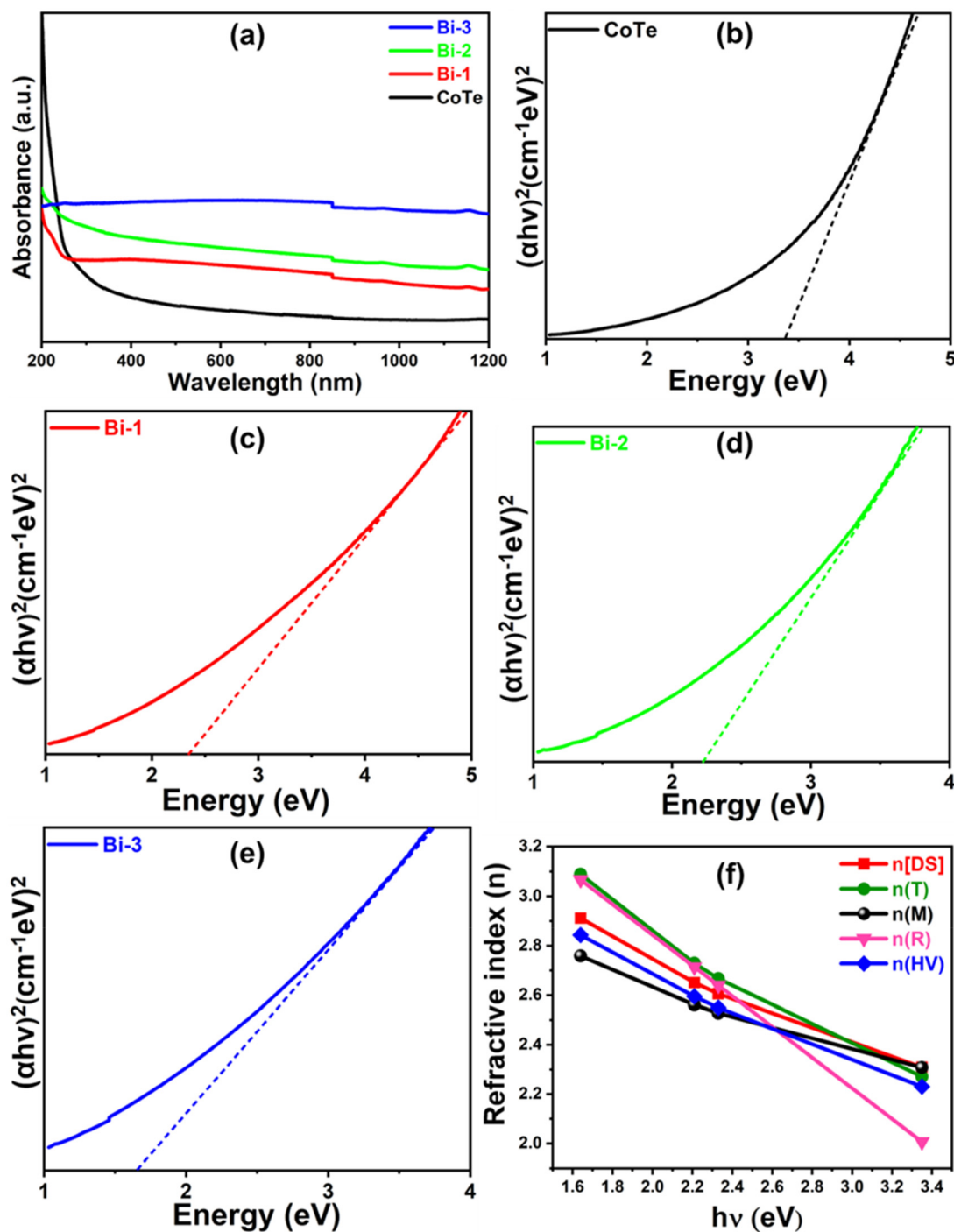
Fig. 9 (a) Absorbance spectra and Tauc plot of (b) CoTe, (c) Bi-1, (d) Bi-2, and (e) Bi-3 samples, and (f) refractive index of the samples from different models.

conductors and high-index materials.[62,63] All the formulae based on these models are mentioned in Table S2 of the SI. The k value in the Moss model is 95 eV, while the values of constants A and B in Herve–Vandamme are 13.6 and 3.74, respectively.[64] All the values of E_g and n have been evaluated and are mentioned in Table S1 of the SI, and the plot of refractive index with bandgap energy is shown in Fig. 9(f). It can be

distinctly observed that with the decreasing E_g value in the range of 3.35–1.64 eV, the n value of the materials gradually increases in all the models. From all the models, the n value remains in the range of 2.00–3.08. This inverse relationship governs the optical behavior of semiconductors, influencing light absorption, transmission, and reflection properties. Understanding this dependency is essential for developing

high-efficiency solar cells, light-emitting diodes (LEDs), and photonic components.

3.8 Photoresponse study

Understanding the optical and electronic properties of materials, as well as the development and enhancement of optoelectronic devices, depends on photoresponse analysis. Examining how synthesized nanoparticles react to light exposure is the primary objective of this study. Metal tellurides are regarded as interesting candidates for a variety of applications, including photodetectors, solar energy conversion, and thermoelectric systems, because of their unique optical and electrical characteristics.[65] For the photoresponse analysis, the $I \sim V$ characteristic curves of all the samples have been obtained. However, the undoped CoTe sample did not show the photoresponse behaviour even after repetition of the measurement. The behaviour of all the other samples is shown in Fig. 10. All the samples have been analyzed both under the light ON and OFF conditions in the voltage range from −10 to 10 V, as shown in Fig. 10(a–c) for the Bi-1, Bi-2, and Bi-3 samples, respectively. It can be observed that the light current shows more response than the dark current. Additionally, it can be noticed that by increasing the doping concentration of Bi, the current increases and the Bi-3 sample displays the highest current. This might be due to the combined effect of optimal Bi doping on its structural and electrical properties. The generation of photocarriers is increased when the band gap is reduced to 1.6 eV as it enhances light absorption, particularly within the near-infrared spectrum. Also, the morphological improvements and increased crystallinity enable optimal light harvesting and carrier mobility,

which raises photocurrent performance.[66] Moreover, the comparison of light and dark current of the three samples is shown in Fig. 10(d) and (e), respectively. Here, the current values under light ON conditions are observed from 229 μA to 810 μA; on the other hand, those under light OFF conditions are observed in the range from 138 μA to 755 μA. With an increase in Bi concentration, the material becomes more photoresponsive, which suggests better charge carrier dynamics and light–matter interaction. The material can detect lower light intensities and react more quickly to enhanced photoresponse, which makes it perfect for broadband or low-light image sensors.

Resistance is a crucial factor in assessing the performance of devices because it can change dramatically in semiconducting materials in reaction to external factors like light (photoresponse), heat (thermoresistance), or electric fields. It is possible to identify charge transport processes, carrier mobility, and the effects of doping or surface alterations by tracking variations in resistance under various circumstances. The resistance of the materials has been calculated by considering the inverse of slope from the $I \sim V$ plot and found to be 0.054 MΩ, 0.019 MΩ, and 0.013 MΩ for the Bi-1, Bi-2, and Bi-3 samples, respectively. It can be observed that the resistance is low in the case of the highest doped sample. The resistance plots are depicted in Fig. S5 of the SI. Here, the resistance value of the highest doped sample, *i.e.*, Bi-3, shows the lowest resistance among all samples.

There are also so many key parameters, which are calculated for optoelectronic device applications. Among the most important are responsivity (R) and detectivity (D), which provide critical insights into the material's ability to convert light into electrical
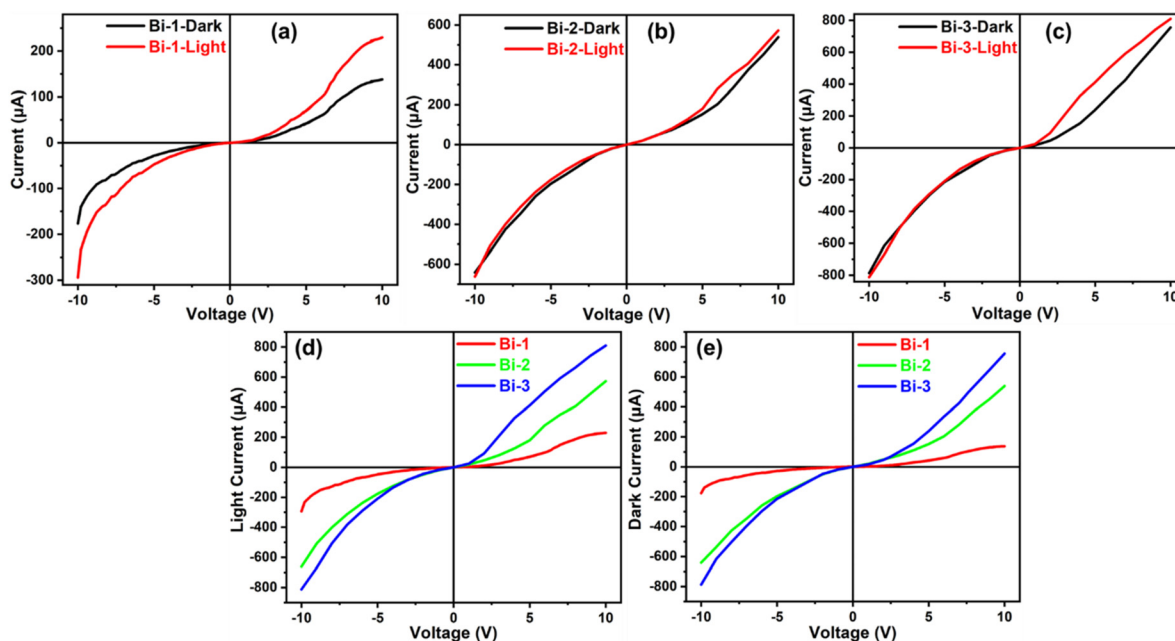

Fig. 10 $I–V$ measurements of (a) Bi-1, (b) Bi-2, and (c) Bi-3 samples under dark and light conditions, (d) light current and (e) dark current comparison of all the samples.

signals and to detect weak optical inputs. R and D of the materials have been calculated using the following relations:[67]

$$R = \frac{I_L}{PA} \qquad (9)$$

and

$$D = R\sqrt{\frac{A}{2eI_D}}. \qquad (10)$$

Here, I_L refers to the light current, P represents the power density, A shows the active area of the photodetector, "e" represents the electron charge, and I_D refers to the dark current. The calculated values are provided in Table 2. The Bi-3 sample experienced high detectivity and responsivity, suggesting effective photocarrier production and collection. This improvement in photoresponse with increasing Bi concentration indicates that Bi doping successfully enhances the optoelectronic performance of the material, underscoring its potential application in photodetector devices.

3.9 NLO study

The nonlinear absorption properties of the material were investigated using the open aperture (OA) Z-scan technique under nanosecond laser excitation at 532 nm. In this method, the material is exposed to an intense laser beam while being translated along the focal plane (Z-axis), allowing for the measurement of nonlinear optical absorption behaviour. The OA Z-scan configuration, which captures changes in transmittance as a function of sample position without an aperture in the detection path, is particularly sensitive to nonlinear absorption processes such as two-photon absorption (TPA), saturable absorption (SA), and reverse saturable absorption (RSA).[68] The total transmitted intensity in the open aperture Z-scan setup has been detected by the PD1 at the time of transmission of the sample through the focal zone of the beam. The OA Z-scan plot of the samples is shown in Fig. 11. The undoped CoTe sample did not exhibit a noticeable OA Z-scan response, indicating negligible nonlinear absorption behaviour. In contrast, the Bi-doped samples, Bi-1, Bi-2, and Bi-3, displayed clear OA Z-scan signatures, confirming the presence of intensity-dependent nonlinear absorption. However, all Bi-doped samples failed to produce significant closed aperture (CA) Z-scan curves, suggesting their absence under the experimental conditions. Fig. 11(a–c) presents the OA curves of Bi-1, Bi-2, and Bi-3 samples, respectively, whereas Fig. 11(d) shows the combined curve of the three samples. The OA Z-scan curves show that when

the Bi content increases, the transmittance gets increasingly deeper. An improvement in the material's nonlinear absorption behaviour is indicated by this narrowing, which shows a greater intensity-dependent absorption close to the focal point. A greater nonlinear absorption coefficient (β) is generally associated with a sharper and deeper valley in the OA curve, indicating that Bi doping successfully boosts the material's capacity to absorb light at high intensities. For applications like optical limiting, where substantial nonlinear absorption is necessary in order to protect highly sensitive optical components from intense laser pulses, this improvement is significant.[69] The transmittance $T(x)$ of the OA curves has been fitted using the relation[70]

$$T(x) = 1 - \frac{I_0 L_{eff}\beta}{2^{\frac{3}{2}}(1 + x^2)} \qquad (11)$$

where x is Z/Z_0. Here, Z represents the sample position and Z_0 refers to the Rayleigh length. I_0 is the irradiance at focus and can be defined as

$$I_0 = \frac{2p}{\pi\omega_0^2} \qquad (12)$$

where p represents the power at focus. ω_0 is the beam waist radius and can be expressed as

$$\omega_0 = \left(\frac{Z_0\lambda}{\pi}\right)^{1/2} \qquad (13)$$

L_{eff} is the effective length of the sample and can be expressed as

$$L_{eff} = \frac{1 - e^{(-\alpha_0 L)}}{\alpha_0} \qquad (14)$$

where L is the thickness of cuvette (1 mm) and α_0 refers to the linear absorption coefficient.

Additionally, β represents the two-photon absorption coefficient and can be written as

$$\beta = \frac{2\sqrt{2}\Delta T}{L_{eff}I_0}. \qquad (15)$$

The open aperture (OA) Z-scan approach was used to successfully extract the nonlinear absorption coefficient (β) for all Bi-doped samples under 532 nm nanosecond laser irradiation. The results showed that there was considerable intensity-dependent absorption behaviour, with the β values for Bi-1, Bi-2, and Bi-3 being 1.402 cm W^{-1}, 1.394 cm W^{-1}, and 1.448 cm W^{-1}, respectively. The Bi-3 sample had the highest β value among all samples, indicating the most nonlinear absorption response. This is probably because of the greater Bi incorporation, which improves light–matter interaction.

However, as none of the samples showed a detectable signal in the CA Z-scan mode, the nonlinear refractive index (n_2) could not be established. The lack of CA curves might suggest that, in the experimental setup, the phase distortion caused by the nonlinear refraction was either insignificant or too minor to be noticed. This implies that the materials are more suited for optical limiting and absorption-based photo-

Table 2 Key parameters of all the samples from photoresponse analysis

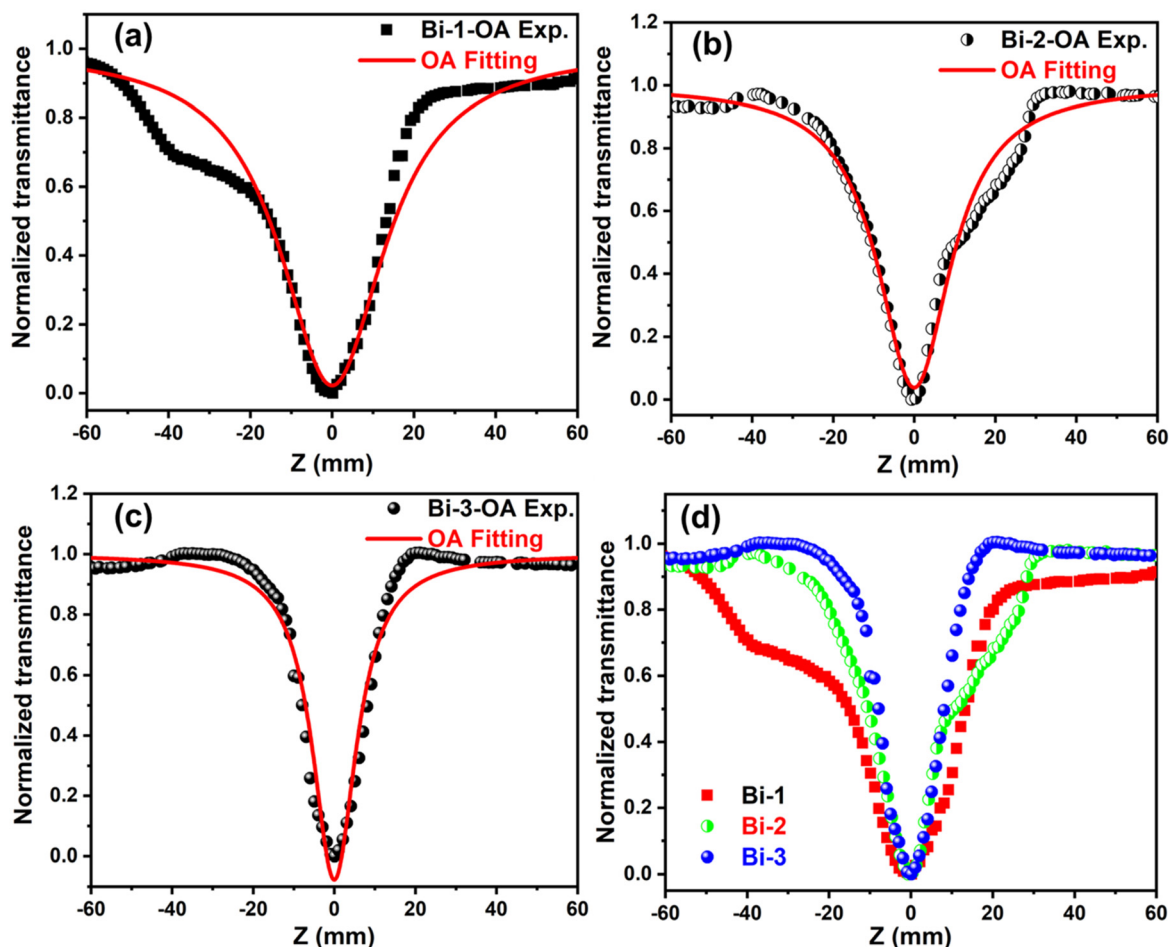| Sample	I_{Light} (μA)	I_{Dark} (μA)	Responsivity (R) (nA W^{-1})	Detectivity (D) (Jones) ($\times 10^9$)
Bi-1	229.69	138.48	141.78	09.04
Bi-2	572.35	537.87	353.30	11.42
Bi-3	810.39	755.93	500.24	13.64

Fig. 11 OA Z-scan fitting of the (a) Bi-1, (b) Bi-2, and (c) Bi-3 samples, and (d) combined curve of all the samples.

nic applications than for refractive nonlinear optics, even though they have notable nonlinear absorption properties and minor nonlinear refractive contributions.[71]

4. Conclusion

Bi-doped CoTe nanoparticles were successfully synthesized *via* a hydrothermal method, with varying Bi doping concentrations to investigate their influence on structural and optical properties. XRD analysis confirmed the formation of a hexagonal CoTe phase ($P63/mmc$ space group), with a noticeable shift toward higher diffraction angles, indicative of Bi incorporation into the lattice. Raman spectroscopy revealed characteristic Te–Te bonding modes along with the A_g Raman-active vibrational mode. FESEM revealed a nanoparticle-like morphology with particle sizes ranging from 20 to 32 nm. XPS confirmed the expected elemental composition, aligning well with the precursor concentrations used in the synthesis. DSC analysis exhibited both endothermic and exothermic peaks with distinct enthalpy values. Optical characterization *via* UV-Vis spectroscopy demonstrated a tunable bandgap ranging from 3.35 eV to 1.64 eV, accompanied by a redshift. Furthermore, the refractive index value gradually increased and found to be in the range of 2.00–3.08. The Bi-3 sample produced the maximum photocurrent of 810 μA under illumination, demonstrating the most improved performance among all the compositions examined, according to the photo-response study. Furthermore, the nonlinear optical characterisation confirms this higher photoactivity. Open aperture Z-scan tests showed that Bi-3 had the highest nonlinear absorption coefficient ($\beta = 1.448$ cm W^{-1}). According to these results, the Bi-3 sample can be considered a prospective candidate for advanced optoelectronic and nonlinear photonic applications since higher Bi doping considerably improves the photoconductive and nonlinear optical capabilities of Bi-doped CoTe materials.

Conflicts of interest

There are no conflicts to declare.

Data availability

All the data related to the present work are included in the manuscript and the SI: FESEM images of all the samples at

1 μm magnification, particle size bar diagrams of all the prepared samples, a TEM image of Bi-3 sample at 50 nm, the DSC pattern of the CoTe sample, resistance plots of Bi-1, Bi-2, and Bi-3 samples, measured E_g values and n (calculated from the E_g value) values of all the prepared samples, and formulae of different models to calculate the refractive index of the material. See DOI: **https://doi.org/10.1039/d5dt01043h**.

Acknowledgements

References

1 J. A. Barreto, W. O. Malley, M. Kubeil, B. Graham, H. Stephan and L. Spiccia, *Adv. Mater.*, 2011, **23**, H18–H40.

2 L. A. Kolahalam, I. V. K. Viswanath, B. S. Diwakar, B. Govindh, V. Reddy and Y. L. N. Murthy, *Mater. Today: Proc.*, 2019, **18**, 2182–2190.

3 M. Nardone, M. Simon, I. V. Karpov and V. G. Karpov, *J. Appl. Phys.*, 2012, **112**, 071101.

4 W. A. Abd El-Ghany, *Phys. Chem. Chem. Phys.*, 2025, **27**, 4567–4586.

5 P. K. Singh and D. K. Dwivedi, *Ferroelectrics*, 2017, **520**, 256–273.

6 S. Rahaman, M. A. Sunil, M. K. Singha and K. Ghosh, *Mater. Res. Express*, 2019, **6**, 106417.

7 M. L. Gallo and A. Sebastian, *J. Phys. D: Appl. Phys.*, 2020, **53**, 213002.

8 S. L. Piano and K. Mayumi, *Appl. Energy*, 2017, **186**, 167–174.

9 L. D. Geoffrion and G. Guisbiers, *Nanoscale Adv.*, 2021, **3**, 4254–4270.

10 C. Li, F. Gao, Y. Wang, L. Zhao, H. Li and Y. Jiang, *Mater. Adv.*, 2022, **3**, 6397–6414.

11 M. Nath, U. De Silva, H. Singh, M. Perkins, W. P. R. Liyanage, S. Umapathi, S. Chakravarty and J. Masud, *ACS Appl. Energy Mater.*, 2021, **4**, 8158–8174.

12 S. Supriya, S. Das, S. Senapati and R. Naik, *J. Am. Ceram. Soc.*, 2023, **106**, 5955–5964.

13 H. Fan, Y. Dai, X. Xue, R. Zheng, Y. Wang, H. Arandiyan, Z. Wang, Z. Shao, H. Sun and Y. Liu, *J. Energy Chem.*, 2024, **97**, 710–737.

14 L. Zhang, Z. Ai, F. Jia, L. Liu, X. Hu and J. C. Yu, *Chem. – Eur. J.*, 2006, **12**, 4185–4190.

15 D. Jamwal and S. K. Mehta, *ChemistrySelect*, 2019, **4**, 1943–1963.

16 Y. Guo, L. Kang, S. Yu, J. Yang, X. Qi, Z. Zhang and Z. Liu, *ChemNanoMat*, 2021, **7**, 323–327.

17 I. U. Arachchige and S. L. Brock, *Acc. Chem. Res.*, 2007, **40**, 801–809.

18 M. Manikandan, K. Subramani, S. Dhanuskodi and M. Sathish, *Energy Fuels*, 2021, **35**, 12527–12537.

19 Y. Liu, Q. Gong, Y. Yin, M. Yi and Y. Liu, *Adv. Funct. Mater.*, 2024, **34**, 2310372.

20 S. Supriya and R. Naik, *2D Metals*, CRC press, 2024.

21 M. S. Khan, M. N. Ashiq, M. F. Ehsan, T. He and S. Ijaz, *Appl. Catal., A*, 2014, **487**, 202–209.

22 J. Guo, Y. Shi, Y. Chu and T. Ma, *Chem. Commun.*, 2013, **49**, 10157–10159.

23 X. Jing, J. Dong, Y. Mao, L. Zhou, J. Ding, H. Dong, L. Zhang, Y. Zhang and W. Zhang, *Inorg. Chem.*, 2024, **63**, 12764–12773.

24 J. Tabassum, N. Baig, M. Sohail, A. Nafady, S. S. A. Shah, A. Ul-Hamid and P. Tsiakaras, *J. Colloid Interface Sci.*, 2024, **658**, 758–771.

25 S. Supriya, S. Senapati and R. Naik, *Next Mater.*, 2025, **7**, 100368.

26 J. Tabassum, N. Baig, M. Sohail, A. Nafady, S. S. A. Shah, A. U. Hamid and P. Tsiakaras, *J. Colloid Interface Sci.*, 2024, **658**, 758–771.

27 Z. M. Alaizeri, H. A. Alhadlaq, S. Aldawood, M. J. Akhtar and M. Ahamed, *ACS Omega*, 2023, **8**, 25020–25033.

28 H. J. Zhang, Q. C. Jia and L. B. Kong, *J. Energy Storage*, 2022, **47**, 103617.

29 O. Schäf, H. Ghobarkar and P. Knauth, *Nanostruct. Mater.*, 2004, **8**, 23–41.

30 G. Qiu, H. Huang, S. Dharmarathna, E. Benbow, L. Stafford and S. L. Suib, *Chem. Mater.*, 2011, **23**, 3892–3901.

31 M. Manikandan, K. Subramani, M. Sathish and S. Dhanuskodi, *RSC Adv.*, 2020, **10**, 13632.

32 S. Supriya, P. C. Kumar, M. Pradhan and R. Naik, *ACS Appl. Mater. Interfaces*, 2024, **16**, 33806–33818.

33 E. K. Kim, H. T. Bui, N. K. Shrestha, C. Y. Shin, S. A. Patil, S. Khadtare, C. Bathula, Y. Y. Noh and S. H. Han, *Electrochim. Acta*, 2018, **260**, 365–371.

34 N. Umeyama, M. Tokumoto, S. Yagi, M. Tomura, K. Tokiwa, T. Fujii, R. Toda, N. Miyakawa and S. I. Ikeda, *Jpn. J. Appl. Phys.*, 2012, **51**, 053001.

35 S. Supriya, S. Das, S. Senapati and R. Naik, *Surf. Interfaces*, 2024, **44**, 103823.

36 R. S. Das and Y. K. Agrawal, *Vib. Spectrosc.*, 2011, **57**, 163–176.

37 P. Rostron, S. Gaber and D. Gaber, *Int. J. Eng. Res. Technol.*, 2016, **6**, 2454–4698.

38 F. Gao, Q. Fu, Y. Ruan, C. Li, Y. Wang, H. Li, J. Li and Y. Jiang, *Adv. Sci.*, 2025, **12**, 2414895.

39 H. Zhang, G. Wang, Z. Zhang, J. H. Lei, T. M. Liu, G. Xing, C. X. Deng, Z. Tang and S. Qu, *Light: Sci. Appl.*, 2022, **11**, 113.

40 S. Supriya, S. Das, S. K. Samal, S. Senapati and R. Naik, *Nanoscale*, 2024, **16**, 7566–7581.

41 A. Padmanaban, T. Dhanasekaran, S. Dhanavel, R. Manigandan, M. Senthil Pandian, P. Ramasamy and D. Balaganesh, *J. Mater. Sci.: Mater. Electron.*, 2022, **33**, 9358–9367.

42 S. Das, S. Senapati, G. K. Pradhan, S. Varadharajanperumal and R. Naik, *ACS Appl. Nano Mater.*, 2023, **6**, 5298–5312.

43 S. Supriya, M. Mallik, A. Parida and R. Naik, *ChemNanoMat*, 2024, **11**, e202400516.

44 L. Chen, Y. Xu, G. Cao, H. M. K. Sari, R. Duan, J. Wang, C. Xie, W. Li and X. Li, *Adv. Funct. Mater.*, 2021, **32**, 2107838.

45 F. Ren, Z. Zhang, Z. Liang, Y. Shen, X. Wang, Q. Chen and Y. Du, *J. Colloid Interface Sci.*, 2022, **616**, 316–325.

46 C. Zhang, H. Li, X. Zeng, S. Xi, R. Wang, L. Zhang, G. Liang, K. Davey, Y. Liu, L. Zhang, S. Zhang and Z. Guo, *Adv. Energy Mater.*, 2022, **12**, 2202577.

47 S. Dubuis, S. H. Messaddeq, Y. Ledemi, A. Côté and Y. Messaddeq, *Opt. Mater. Express*, 2021, **11**, 2560–2575.

48 B. J. Fernandes, N. Naresh, K. Ramesh, K. Sridharan and N. K. Udayashankar, *J. Alloys Compd.*, 2017, **721**, 674–682.

49 A. T. Muzhanje, M. A. Hassan, S. Ookawara and H. Hassan, *J. Energy Storage*, 2022, **51**, 104353.

50 A. Das, P. Rani, S. G. Dastider, K. K. Mondal and P. S. Alegaonkar, *ChemistrySelect*, 2024, **9**, e202400032.

51 B. R. Dahal, R. P. Dulal, L. L. Pegg and J. Philip, *J. Vac. Sci. Technol., B:Nanotechnol. Microelectron.:Mater., Process., Meas., Phenom.*, 2016, **34**, 051801.

52 P. Kumar and K. Singh, *Cryst. Growth Des.*, 2009, **9**, 3089–3094.

53 M. S. Khan, M. N. Ashiq and M. F. Ehsan, *Appl. Catal.*, 2014, **487**, 202–209.

54 L. Zhao, Y. Tong, J. Yin, H. Li, L. Du, J. Li and Y. Jiang, *Small*, 2024, **20**, 2403861.

55 D. Jamwal, G. Kaur, P. Raizada, P. Singh, D. Pathak and P. Thakur, *J. Phys. Chem. C*, 2015, **119**, 5062–5073.

56 Y. Hu, Y. Cao, P. Wang, D. Li, W. Chen, Y. He, X. Fu, Y. Shao and Y. Zheng, *Appl. Catal., B*, 2012, **125**, 294–303.

57 N. G. Khlebtsov, L. A. Trachuk and A. G. Mel'nikov, *Opt. Spectrosc.*, 2005, **98**, 77–83.

58 M. P. Côté, C. Boukouvala, J. R. Daniel, E. Ringe, D. Boudreau and A. M. Ritcey, *ACS Appl. Nano Mater.*, 2024, **7**, 8783–8791.

59 N. K. Sahoo, S. Thakur and R. B. Tokas, *J. Phys. D: Appl. Phys.*, 2006, **39**, 2571–2579.

60 V. Dimitrov and S. Sakka, *J. Appl. Phys.*, 1996, **79**, 1736–1740.

61 E. Sharma and P. Sharma, *Mater. Today: Proc.*, 2020, **28**, 92–95.

62 S. K. Tripathy, *Opt. Mater.*, 2015, **46**, 240–246.

63 I. Sharma, S. K. Tripathi and P. B. Barman, *J. Appl. Phys.*, 2011, **110**, 043108.

64 H. M. H. Zakaly, S. A. M. Issa, H. A. Saudi, M. Algethami and T. S. Soliman, *Opt. Mater.*, 2024, **152**, 115496.

65 A. Purkayastha, S. Kim, D. D. Gandhi, P. G. Ganesan, T. Borca-Tasciuc and G. Ramanath, *Adv. Mater.*, 2006, **18**, 2958–2963.

66 S. Khan, S. Daemi, M. Kanwal, C. Xiao and F. E. Osterloh, *J. Mater. Chem. A*, 2023, **11**, 23418–23429.

67 S. Supriya, S. Das, A. Parida and R. Naik, *Mater. Res. Bull.*, 2025, **189**, 113486.

68 M. Mayilmurugan, G. Rajamanickam, R. Perumalsamy and D. Sivasubramanian, *ACS Omega*, 2022, **7**, 14556–14561.

69 J. Lee, Y. I. Jhon, K. Lee, Y. M. Jhon and J. H. Lee, *Sci. Rep.*, 2020, **10**, 15305.

70 S. K. Patra, B. K. Dadhich, B. Bhushan, R. K. Choubey and A. Priyam, *ACS Omega*, 2021, **6**, 31375–31383.

71 K. John U and S. Mathew, *Appl. Phys. A*, 2022, **128**, 259.